12th International Conference on Fracture Mechanics of Concrete and Concrete Structures
FraMCoS-12
B.L.A. Pichler, Ch. Hellmich, P. Preinstorfer (Eds)

https://doi.org/10.21012/FC12.1186
MS07-1:4

# NON-DESTRUCTIVE DETECTION OF HOLLOW-PARTICLE-MIXED FILLER PUT INTO CONCRETE CRACKS USING INFRARED THERMOGRAPHY AND HEAT FLUX SIMULATION

**TAIKI HAGIWARA[*] AND TETSUYA SUZUKI[†]**

[*] Civil Engineering Research Institute for Cold Region, Public Works Research Institute
Hiragishi 1-34, Toyohira-ku, Sapporo City, Hokkaido 062-8602, Japan
e-mail: t.hagiwara8220@outlook.com

[†] Institute of Agriculture, Niigata University
2-no-cho 8050, Ikarashi, Nishi-ku, Niigata City, Niigata 950-2181, Japan
e-mail: suzuki@agr.niigata-u.ac.jp

**Key words:** Repair of Concrete Cracks, Hollow Particle Mixed Filler, Filling Proportion, Non-Destructive Testing, Infrared Thermography, Heat Conduction Simulation

**Abstract:** Filler into concrete cracks is one of the repair methods for in-service concrete structures. Applying epoxy-based filler to the structures combines concrete material with epoxy resin and protects re-degradation. However, the insufficient filling of the filler into cracks can reduce the repair effectiveness. By the authors, epoxy-based filler mixed with hollow particles has been developed for improving mechanical properties of the repaired concrete and inspecting the insufficient filling well. In particular, this study focuses on non-destructive detection of the insufficient filling of the mixed filler into an artificial concrete crack using active infrared thermography. In lab experiment, we performed active infrared thermography with 20-minute heating and 40-minute cooling for four concrete samples. The concrete samples had an artificial crack that was filled with epoxy-based filler mixed with hollow particles. Each filling proportion into the crack was set to 20%, 50%, 80%, and 100%. The volume ratio of the epoxy resin to the hollow particles in the filler was 2 to 1. In analysis, we analyze the surface temperature fields of the samples using thermal images and the inner temperature fields using a two-dimensional heat conduction simulation. As a result, in the 20%-filling sample, which has the smallest filling proportion, the standard deviations of the filler temperatures during first 60 seconds of the cooling are largest in the samples. Additionally, in the same sample, changes of the heat flux in the depth direction around the surface, which is determined by the simulation, are also largest. The characteristics of the temperature variation and heat conduction probably depend on the hollow particles. The filler mixed with the hollow particles enables us to detect the filling into the crack accurately, quickly, and remotely. Thus, this study provides the non-destructive method for monitoring the repair using the hollow particle mixed filler.

## 1 INTRODUCTION

One common repair method for concrete structures involves filling cracks with specialized repair materials. Epoxy-based crack repair is frequently employed for this purpose [1-4]. By injecting epoxy resin into the cracks, the material not only shields the structure from further deterioration but also enhances its mechanical strength by bonding the concrete and resin. The authors have developed an epoxy resin mixed with hollow particles to improve both the physical

properties of the repair material and the accuracy of post-repair inspection of filling proportions [5, 6]. Hollow particles are utilized across various technical fields [7-18], and their incorporation into epoxy resins has been widely studied [19-25]. Numerous reports have highlighted the improvement of mechanical properties through the inclusion of particles in composite materials [26-31]. A key challenge in crack repair is the presence of unfilled voids, which can lead to the re-degradation of repaired structures. An added benefit of incorporating hollow particles into the filler is the reduction in heat capacity, making the material more responsive to temperature changes. This thermal responsiveness allows for the rapid evaluation of filling completeness, thereby improving inspection accuracy. In this study, infrared thermography—a non-destructive method widely used for monitoring concrete structures [32-35]—is applied. The authors previously proposed a non-contact method to detect unfilled areas in repaired cracks using infrared thermography [36].

This study aims to evaluate the filling proportions of hollow particle-modified epoxy resin through a combination of non-destructive infrared thermography and heat conduction simulations. The simulations provide detailed insights into the thermal behavior of the filler material. A laboratory-scale experiment was conducted using four types of test samples, each containing artificial cracks filled with hollow particle-modified resin. The focus of this research is the non-destructive detection of insufficient filler penetration using active infrared thermography to assess filling proportions accurately.

## 2 EXPERIMENTAL METHODS

### 2.1 Test samples

Test samples with artificial cracks filled using a hollow particle-modified filler were prepared as part of this study. The filler consisted of epoxy resin and hollow particles (3M), mixed at a volume ratio of 2:1 (see Figure 1). The specifications of the filler material are detailed in Table 1. Artificial

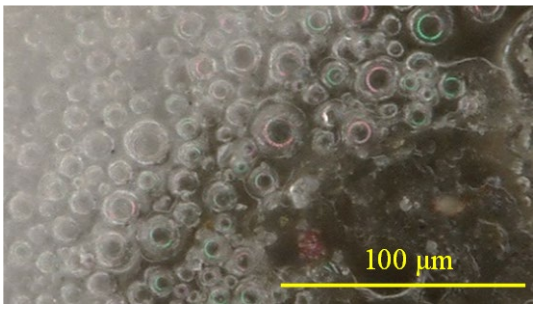


**Figure 1**: Hollow particle mixed filler in this study.

**Table 1**: Filler specification

| | Mixture rate (%) | Viscosity (mPa・s) | Tensile strength ($N/mm^2$) | Elongation rate (%) | Specific gravity |
|---|---|---|---|---|---|
| HPG | 50 | 6,800 | 1.21 | 29.9 | 0.89 |

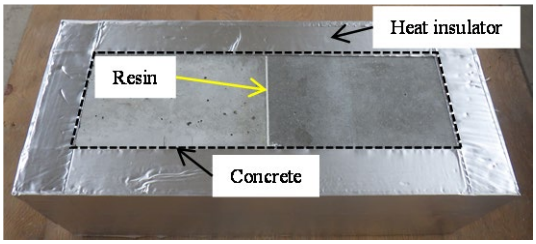


**Figure 2**: An appearance of the test samples.

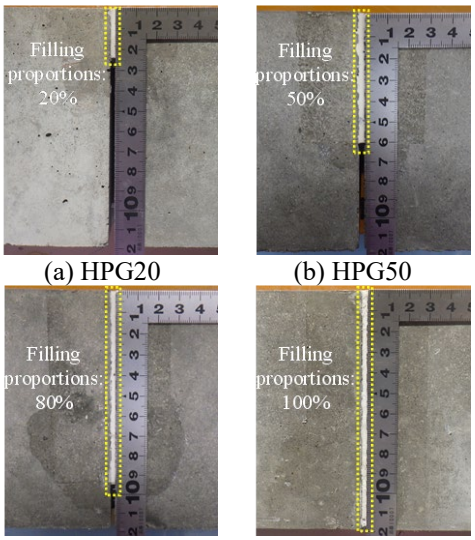


(a) HPG20 (b) HPG50

(c) HPG80 (d) HPG100

**Figure 3**: Different filling proportions.

cracks, 2 mm in width, were created between two concrete blocks, each measuring 200 mm in width, 120 mm in depth, and 120 mm in height. The appearance of the samples with these artificial cracks is shown in Figure 2. These cracks were then filled with the hollow particle-modified filler. Figure 3 illustrates the different filling proportions observed from the side view of the samples.

As described in Section 2.2, each sample

was wrapped with heat-insulating material and aluminum tape to minimize heat transfer from the sides and bottom during the heating and cooling experiments.

Four experimental cases were designed, each with a different filling proportion. The artificial cracks had a total height of 120 mm, while the filler was applied to varying heights: 24 mm for 20% filling, 60 mm for 50% filling, 96 mm for 80% filling, and 120 mm for 100% filling. These cases are referred to as HPG20, HPG50, HPG80, and HPG100 throughout this study.

### 2.2 Infrared thermography

An infrared thermography camera was used to measure the surface temperatures of the samples and to detect the filling proportions using an active thermography method. In this method, the object is subjected to an external thermal load, inducing temperature fluctuations that are captured for analysis. The experimental setup for the active thermography method is illustrated in Figure 4.

In addition to infrared imaging, temperature measurements were conducted using thermocouples installed at six specific locations on each sample. These locations included the surface, middle, and ends of both the resin and concrete sections, ensuring comprehensive thermal profiling.

The samples were heated using two 900 W heaters for 20 minutes, followed by a cooling period of 40 minutes with the heaters turned off. The infrared thermography camera was positioned 0.3 meters from the sample surface, capturing thermal images at intervals of one image every 10 seconds. Simultaneously, the thermocouples recorded temperature data at the same 10-second intervals to complement the infrared measurements.

## 3 ANALYTICAL METHODS

### 3.1 Heat conduction simulation

The heat transfer inside each sample during the heating and cooling process of the active method is analyzed by a numerical simulation of two-dimensional unsteady heat conduction.

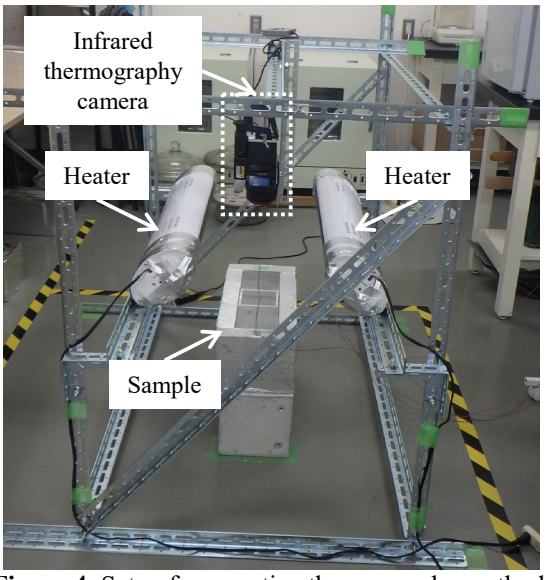


**Figure 4**: Setup for an active thermography method.

Considering the symmetry of each sample, which consists of two concrete blocks of the same size, a two-dimensional calculation model is set up with the spatial range covering half of each sample in the horizontal and vertical directions as shown in Figure 5. The two-dimensional unsteady heat conduction equation is as follows:

$$\rho c(\partial T/\partial t) = \lambda(\partial^2 T/\partial x^2 + \partial^2 T/\partial y^2), \quad (1)$$

where $T$ is temperature (K), $t$ is time (s), $x$ is horizontal position (m), $y$ is vertical position (m), $\rho$ is density (kg/m$^3$), $c$ is specific heat (J/(kg·K)) and $\lambda$ is thermal conductivity (W/(m·K)).

In the discretization of Equation (1), a simple difference method is used. As shown in Figure 5, the discretization is unequally spaced along the horizontal x-axis and equally spaced along the vertical y-axis. We numerically solve the equation with the explicit method. The time step $\Delta t$ is set to 0.01 s, and the space steps $\Delta x$ and $\Delta y$ are set to 0.001 m to satisfy the stability of the explicit method. As unequal intervals in the horizontal x-axis direction, $\Delta x$ is given for a width of 31 mm from the origin of the calculation space, $5\Delta x$ for the next 30 mm width, and $10\Delta x$ for the next 140 mm width. The initial condition is given the temperatures at the start of heating measured by the thermocouples. For four boundary conditions, one temperature boundary is given on the model surface at $y = 0$ using the

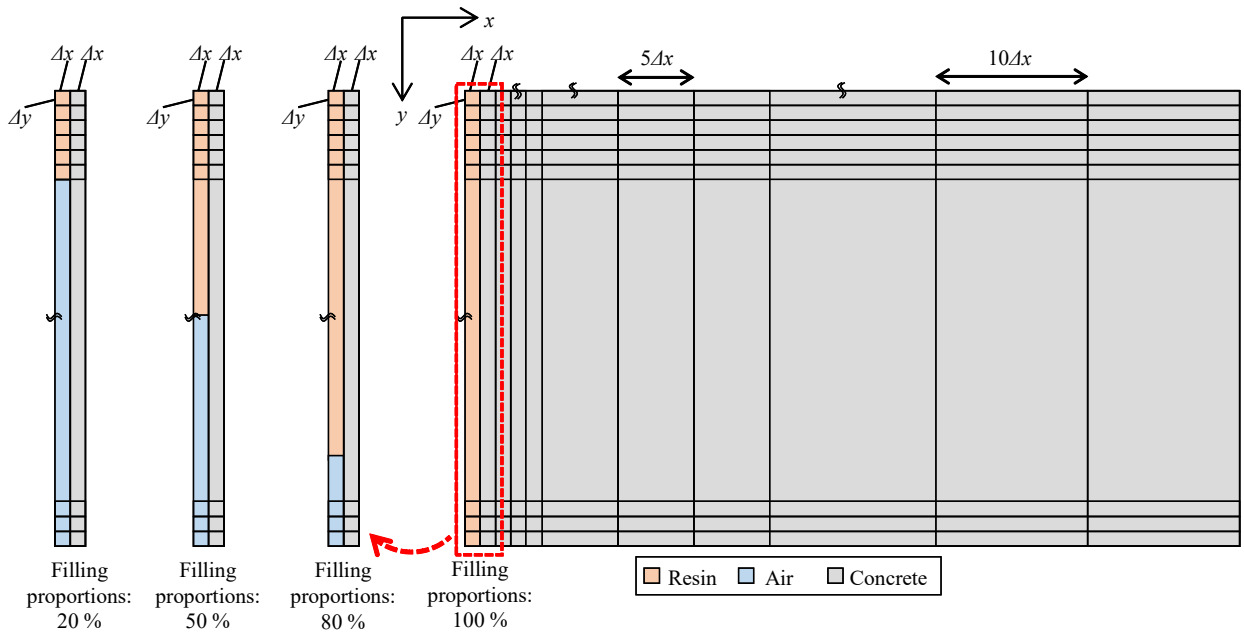


**Figure 5**: Two-dimensional simulation model for unsteady heat conduction inside the test samples.

thermocouple temperatures during the active method, and the other boundaries are given the adiabatic condition on the two sides and the bottom of the model.

### 3.2 Thermal properties

The thermophysical properties utilized in the heat conduction simulation are presented in Table 2. The specific heat capacity and thermal conductivity values for concrete were obtained by averaging the data reported in references [37, 38]. The apparent thermophysical properties of the hollow particle-epoxy resin mixture were determined by modeling it as a porous composite consisting of epoxy resin and air, following the approach outlined in reference [39].

### 3.3 Thermal image processing

The analysis area of the thermal images acquired through the active thermography method is illustrated in Figure 6. As shown, the region surrounding the thermocouple installed on the resin surface is excluded from the analysis. Instead, two separate regions, each comprising 50 pixels from the resin area, are selected, resulting in a total of 100 pixels for analysis. These regions are extracted from each thermal image captured during the experiment, and the temperature variations on the resin surface are subsequently evaluated.

**Table 2**: Thermophysical properties

| Material | Density (kg/m$^3$) | Specific heat (J/(kg·K)) | Thermal conductivity (W/(m·K)) |
|---|---|---|---|
| Concrete [37, 38] | 2,400 | 1,155 | 2.7 |
| Air [37] | 1.1763 | 1,007 | 0.02614 |
| Epoxy resin [37] | 1,850 | 1,100 | 0.3 |
| Hollow particle mixed filler | 926 | 1,100 | 0.14 |

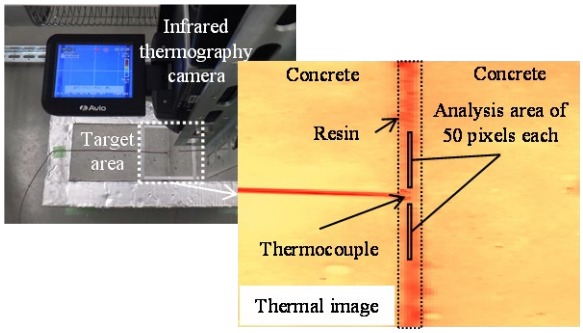


**Figure 6**: Analysis area of thermal image processing.

## 4 RESULTS

### 4.1 Temperature characteristics inside the samples

Figure 7 illustrates the temperature variations of the samples, as measured by the thermocouples during the active thermography

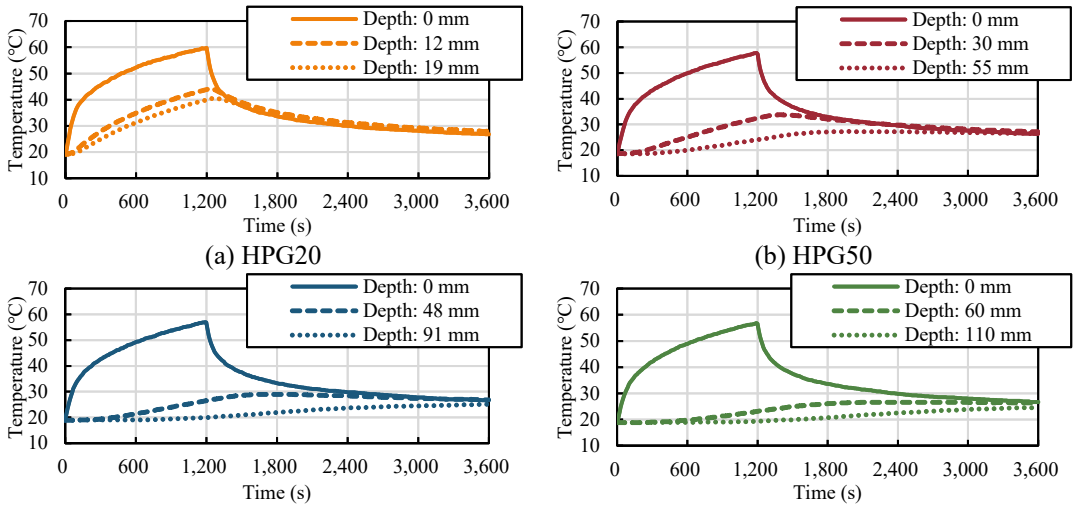


(a) HPG20 (b) HPG50

(c) HPG80 (d) HPG100

**Figure 7**: Temperature variations in each sample measured by thermocouples.

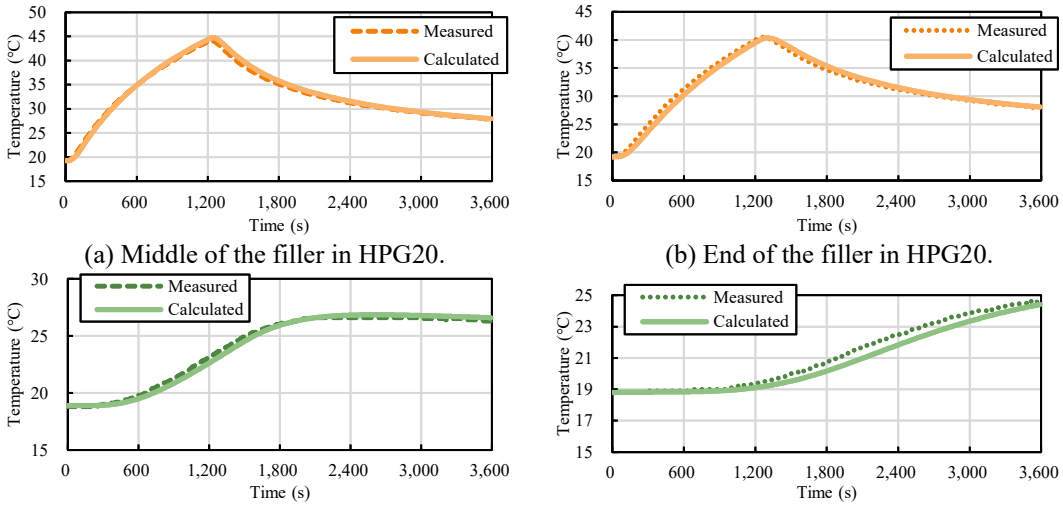


(a) Middle of the filler in HPG20. (b) End of the filler in HPG20.

(c) Middle of the filler in HPG100. (d) End of the filler in HPG100.

**Figure 8**: Results of the heat conduction simulation in HPG20 and HPG100.

process. The heating phase occurs before 1,200 seconds, while the cooling phase begins after 1,200 seconds. During the heating phase, the temperatures of the resin surfaces increase, whereas they decrease during the cooling phase. The internal temperatures of the samples reach their peak values later than the surface temperatures, reflecting the thermal lag as the thermocouple positions move deeper into the samples.

Figure 8 presents a comparison between the resin temperatures measured by the thermocouples and those calculated using the heat conduction simulation for HPG20 and HPG100. The simulation results for both HPG20 and HPG100 closely align with the corresponding measured values, demonstrating the accuracy of the heat conduction model.

### 4.2 Evaluation of resin fill proportions with infrared thermography

The mean values and standard deviations of temperatures extracted from the analysis areas of the thermal images (refer to Figure 6) are presented in Figure 9. In Figure 9(a), no significant differences are observed in the average temperatures across the different cases. Considering that variations in filling proportions correspond to differences in the heat capacity of the samples, it can be expected that samples with lower filling proportions will exhibit more rapid temperature changes due to their reduced heat capacity.

We focus on the temporal variation of the standard deviations within each analysis area, as shown in Figure 9(b), which serves as an indicator of thermal variation during the cooling process. Here, standard deviation is defined as SD. To detect differences in filling proportions within a relatively short time frame, particular attention is given to the rapid changes in standard deviation during the first 60 seconds of the cooling phase, from 1,200 s to 1,260 s.

Figure 10 illustrates the time-dependent variations in standard deviation (SD), comparing values at 1,200 s with those at subsequent time points from 1,210 s to 1,260 s during cooling. The changes in SD over the first 10 seconds (from 1,200 s to 1,210 s) are as follows: HPG20: −0.18 °C (from 1.16 °C to 0.98 °C), HPG50: −0.18 °C (from 0.67 °C to 0.49 °C), HPG80: −0.14 °C (from 0.60 °C to 0.46 °C), and HPG100: −0.15 °C (from 0.48 °C to 0.34 °C). These variations are relatively small across all cases in the first 10 seconds. For the 30-second interval (from 1,200 s to 1,230 s), the SD variations are: HPG20: −0.43 °C (from 1.16 °C to 0.73 °C), HPG50: −0.34 °C (from 0.67 °C to 0.33 °C), HPG80: −0.26 °C (from 0.60 °C to 0.34 °C), and HPG100: −0.25 °C (from 0.48 °C to 0.23 °C). At this point, the difference between HPG20 and HPG50 becomes more pronounced. Over the 60-second period (from 1,200 s to 1,260 s), the SD variations are: HPG20: −0.55 °C (from 1.16 °C to 0.61 °C), HPG50: −0.36 °C (from 0.67 °C to 0.31 °C), HPG80: −0.39 °C (from 0.60 °C to 0.21 °C), and HPG100: −0.21 °C (from 0.48 °C to 0.26 °C). In the 60-second interval, it is evident that lower filling proportions correspond to larger variations in standard deviation, indicating greater thermal responsiveness in underfilled samples. This phenomenon is further discussed in Section 4.3 using heat flux data obtained from the heat conduction simulations.

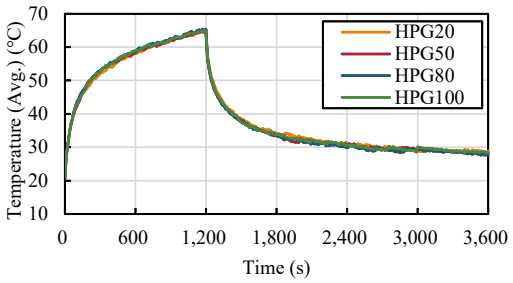


(a) Time-series of the average temperature.

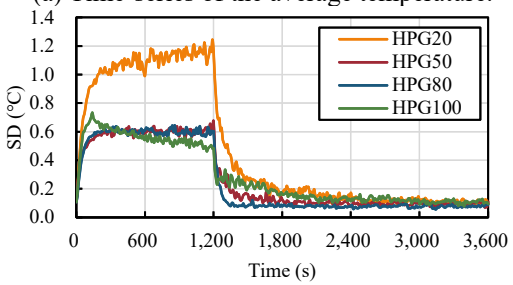


(b) Time-series of the standard diviation (SD).

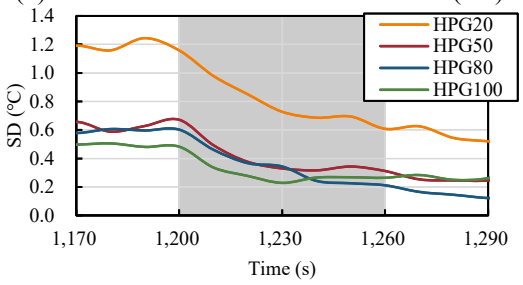


(c) Time-series of the SD immediately after the start of the cooling.

**Figure 9**: Time-series of the average temperature and standard deviation in each analysis area of the thermal images.

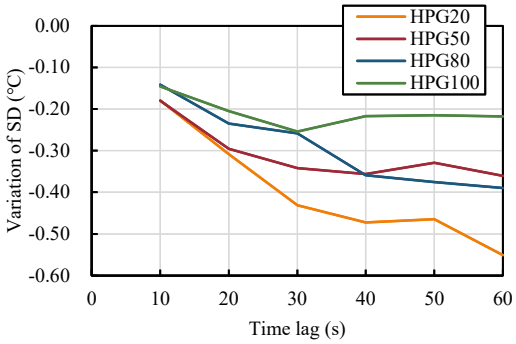


**Figure 10**: Variations over time between the SD at 1,200 s and the one at each time point from 1,210 s to 1,260 s in the cooling. process.

### 4.3 Heat flux characteristics inside the samples depending on resin filling proportion

This study also focuses on the temperature and heat flux fields within each sample. Figure 11 presents the vertical heat flux at a depth of

1 mm beneath the surface of each sample during the first 60 seconds of the cooling phase (from 1,200 s to 1,260 s). In this figure, positive values indicate downward heat flux (toward the bottom of the sample), while negative values represent upward heat flux (toward the surface). Considering the vertical spatial resolution of the simulation, we specifically analyze the changes in heat flux at a depth of 1 mm near the surface.

Figure 12 shows the variations in heat flux over different time intervals. For the initial 10 seconds of cooling (from 1,200 s to 1,210 s), the changes in heat flux are as follows: HPG20: −1,740 W/m² (from 3,749 W/m² to 2,009 W/m²), HPG50: −1,618 W/m² (from 3,538 W/m² to 1,921 W/m²), HPG80: −1,608 W/m² (from 3,781 W/m² to 2,172 W/m²), and HPG100: −1,465 W/m² (from 2,263 W/m² to 798 W/m²). These variations over 10 seconds are relatively small across all cases. For the 30-second interval (from 1,200 s to 1,230 s), the heat flux variations are: HPG20: −3,685 W/m² (from 3,749 W/m² to 64 W/m²), HPG50: −3,244 W/m² (from 3,538 W/m² to 294 W/m²), HPG80: −3,247 W/m² (from 3,781 W/m² to 534 W/m²), and HPG100: −2,677 W/m² (from 2,263 W/m² to −414 W/m²). These changes are more pronounced compared to the 10-second interval. Over the full 60-second period (from 1,200 s to 1,260 s), the variations in heat flux are: HPG20: −4,430 W/m² (from 3,749 W/m² to −681 W/m²), HPG50: −4,032 W/m² (from 3,538 W/m² to −494 W/m²), HPG80: −3,902 W/m² (from 3,781 W/m² to −121 W/m²), and HPG100: −3,062 W/m² (from 2,263 W/m² to −799 W/m²). The largest change in heat flux over 60 seconds is observed in HPG20, which has the lowest filling proportion. Similar trends were observed at a depth of 3 mm.

In HPG20, the temperature at the resin's end begins to decrease immediately after the start of cooling (see Figure 7(a)), indicating that heat conduction toward the end of the resin occurs during the heating phase. This suggests that in HPG20, heat conduction is more likely directed toward the surface during cooling. For the other cases (HPG50, HPG80, and HPG100), the maximum temperatures are reached within the resin shortly after the

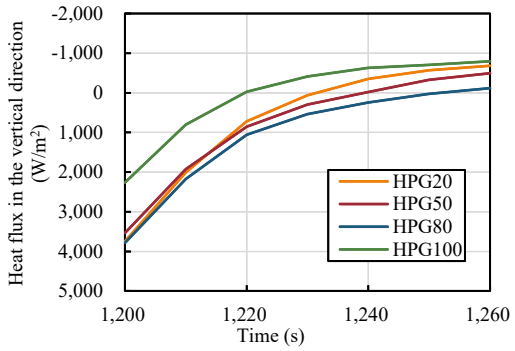


**Figure 11**: Time-series of the heat flux in the vertical direction calculated by the simulation. Positive values are in the vertical downward and negative values are in the vertical upward.

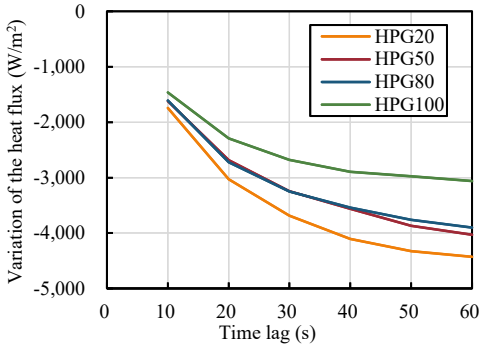


**Figure 12**: Variations over time between the heat flux at 1,200 s and the one at each time point from 1,210 s to 1,260 s in the cooling process.

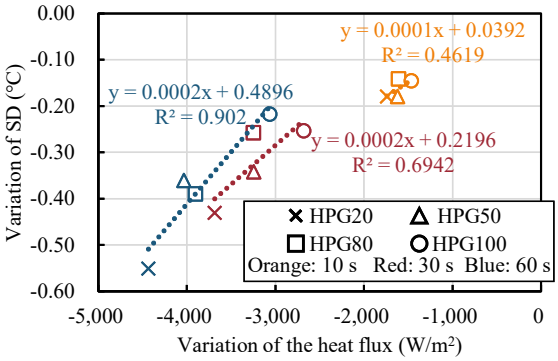


**Figure 13**: Relationship between the variations of heat flux and SD from 1,200 s to 1,260 s in the cooling process.

cooling phase begins (see Figures 7(b), 7(c), and 7(d)), indicating predominant downward heat conduction. Furthermore, the addition of hollow particles reduces the thermal conductivity in HPG20, making heat conduction toward the surface more pronounced. Figure 13 illustrates the relationship between variations in heat flux and standard deviation (SD) from 1,200 s to

1,260 s during cooling. Insufficient filling of the resin results in larger temporal variations in temperature (i.e., larger SD values) shortly after the cooling process begins. This behavior, particularly evident in HPG20, can be attributed to the heat flux dynamics within the sample.

## 5 DISCUSSION

### 5.1 Implications for field applications with unknown crack depth

This section discusses implications for field applications using our proposed method. Firstly, for field testing, the use of an infrared thermography camera is essential. When direct access to target structures is feasible, the camera can be mounted on a single tripod or a tripod setup. For instance, the camera used in this study weighs x g, making it lightweight and portable enough for on-site inspections. However, in situations where direct access to target structures is difficult—such as high, remote, or hazardous locations—an unmanned aerial vehicle (UAV) equipped with a thermography camera can be employed. This approach allows for data acquisition in areas that are otherwise inaccessible or risky. A limitation of this study is that validation was conducted only at a fixed measurement distance of 30 cm. In field conditions where it is challenging to position the camera close to the target, a thermography camera with higher resolution will be required to maintain measurement accuracy over greater distances.

Secondly, while this study employs an active thermography method, passive thermography is recommended for field applications due to its practicality. For cracks with unknown depths, the surface temperature field can be analyzed by calculating the heat flux balance under real-world meteorological conditions. In simulations, an assumed crack depth is set, and the ideal temperature field is calculated. By simulating temperature fields under various assumed crack depths, the optimal depth corresponding to the measured surface temperatures of the target structure can be identified.

In our previous studies, passive thermography methods combined with heat balance simulations were successfully applied to steel structures [40] and dam structures [41], demonstrating the feasibility of this approach in diverse field conditions.

### 5.2 Implications for concrete fracture

This section discusses the implications of our method for addressing concrete fractures. The use of hollow particle-modified filler is designed not only to enhance the mechanical properties of repaired structures but also to facilitate the inspection of filler penetration into cracks. Our previous research demonstrated improvements in the tensile properties of mortar bars repaired with hollow particle-modified filler, as verified through ultrasonic testing and acoustic emission techniques [6]. While these findings were based on lab-scale experiments, the filler is expected to similarly enhance the mechanical performance of in-service repaired structures. The method proposed in this study focuses on the inspection of filler penetration in in-service structures using infrared thermography. For future work, we aim to achieve non-contact detection of resin filling rates across multiple cracks over large surface areas using thermal imaging techniques. This will enable efficient, large-scale inspections of repaired concrete structures.

## 6 CONCLUSIONS

This study focuses on the non-destructive detection of insufficient filling of hollow particle-modified filler in artificial concrete cracks using active infrared thermography. In the experiments, test samples were prepared with 2-mm wide artificial cracks filled with varying amounts of filler. The samples were subjected to controlled heating and cooling using the active thermography method, with filling proportions set at 20%, 50%, 80%, and 100%. The temperature data obtained from the thermal images were used to evaluate the filling proportions, contributing to improved

inspection accuracy. The key findings are summarized below:

1) The two-dimensional unsteady heat conduction simulation successfully reproduced the temperature fluctuations within the samples during both the heating and cooling processes.
2) The standard deviation, representing thermal image variation, exhibited larger fluctuations within the first 60 seconds of cooling for samples with lower filling proportions. This suggests that the use of hollow particle-modified filler enhances inspection accuracy by enabling quicker detection of insufficient filling.
3) In the case of HPG20 (20% filling), the largest changes in vertical heat flux were observed during the first 60 seconds of cooling. This indicates that greater temporal variations in the standard deviation of thermal images are associated with lower filling proportions.
4)

## REFERENCES


[1] Issa, C.A. and Debs, P., 2007. Experimental study of epoxy repairing of cracks in concrete. *Construction and Building Materials*. **21**, 157-163.

[2] Ahmad, S., Elahi, A., Barbhuiya, S. and Farooqi, Y., 2013. Repair of cracks in simply supported beams using epoxy injection technique. *Materials and Structures*. **46**, 1547-1559.

[3] Griffin, S., Askarinejad, H. and Farrant, B., 2017. Evaluation of epoxy injection method for concrete crack repair. *International Journal of Structural and Civil Engineering Research*. **6**(3), 177-181.

[4] Modesti, L.A., Vargas, A.S. and Schneider, E.L., 2020. Repairing concrete with epoxy adhesives. *International Journal of Adhesion and Adhesives*. **101**, 102645.

[5] Kojima, A., Takahashi, K., Suzuki, T. and Fujii, N., 2018. Evaluation of filling proportions of hollow particle mixed filler using infrared images (in Japanese). *Proceedings of the Japan Concrete Institute*. **40**(1), 1803-1808.

[6] Takahashi, K., Suzuki, T. and Fujii, N., 2019. Evaluation of tensile fracture characteristics of hollow particle mixed filler and mortar composites using an acoustic emission method (in Japanese). *Proceedings of the Japan Concrete Institute*. **41**(1), 1613-1618.

[7] Gupta, N. and Nagorny, R., 2006. Tensile properties of glass microballoon-epoxy resin syntactic foams. *Journal of Applied Polymer Science*. **102**, 1254-1261.

[8] Yung, K.C., Zhu, B.L., Yue, T.M. and Xie, C.S., 2009. Preparation and properties of hollow glass microsphere-filled epoxy-matrix composites. *Composites Science and Technology*. **69**, 260-264.

[9] Zhu, B., Ma, J., Wang, J., Wu, J. and Peng, D., 2012. Thermal, dielectric and compressive properties of hollow glass microsphere filled epoxy-matrix composites. *Reinforced Plastics and Composites*. **31**(19), 1311-1326.

[10] Gupta, N., Zeltmann, S.E., Shunmugasamy, V.C. and Pinisetty, D., 2014. Applications of polymer matrix syntactic foams. *The Journal of The Minerals, Metals & Materials Society (TMS)*. **66**, 245-254.

[11] Ramli R.A., 2017. Hollow polymer particles: a review. *The Royal Society of Chemistry*. **7**, 52632-52650.

[12] Karasu, B., Demirel, İ., Öztuvan, A. and Özdemir, B., 2019. Glass microspheres. *El-Cezeri*, **6**(3), 613-641.

[13] Sharma, J. and Polizos, G., 2020. Hollow silica particles: recent progress and future perspectives. *Nanomaterials*, **10**(8), 1599.

[14] Afolabi, L. O., Ariff, Z. M., Hashim, S. F. S., Alomayri, T., Mahzan, S., Kamarudin, K. A., and Muhammad, I. D., 2020. Syntactic foams formulations, production techniques, and industry applications: A review. *Journal of Materials Research and Technology*, **9**(5), 10698-10718.

[15] Tang, T., Yuan, Y., Yalikun, Y., Hosokawa, Y., Li, M., and Tanaka, Y., 2021. Glass based micro total analysis systems: Materials, fabrication methods, and applications. *Sensors and Actuators B: Chemical*, **339**, 129859.

[16] He, Z.Q., Yang, Y., Yu, B., Yang, J.P., Jiang, X.B., Tian, B., Wang, M., Li, X.Y., Sun, S.Q. and Sun, H. 2022. Research on properties of hollow glass microspheres/epoxy resin composites applied in deep rock in-situ temperature-preserved coring. *Petroleum Science*. **19**, 720-730.

[17] Santos, J. P., Correia, D. S., Marques, E. A., Carbas, R. J., Gilbert, F., and da Silva, L. F., 2022. Characterization of the effect of hollow glass beads on the mechanical properties of structural adhesives. Materials, **15**(11), 3817.

[18] Mahmoud, M., Kraxner, J., Elsayed, H., Bernardo, E., and Galusek, D., 2023. Fabrication and environmental applications of glass microspheres: A review. *Ceramics International*, **49**, 39745-39759.

[19] Yung, K. C., Zhu, B. L., Yue, T. M., and Xie, C. S., 2009. Preparation and properties of hollow glass microsphere-filled epoxy-matrix composites. *Composites science and technology*, **69**(2), 260-264.

[20] Galvagnini, F., Fredi, G., Dorigato, A., Fambri, L., and Pegoretti, A., 2021. Mechanical behaviour of multifunctional epoxy/hollow glass microspheres/paraffin microcapsules syntactic foams for thermal management. *Polymers*, **13**(17), 2896.

[21] Afolabi, O. A., Kanny, K., and Mohan, T. P., 2021. Processing of hollow glass microspheres (HGM) filled epoxy syntactic foam composites with improved structural characteristics. *Science and Engineering of Composite Materials*, **28**(1), 116-127.

[22] Anirudh, S., Jayalakshmi, C. G., Anand, A., Kandasubramanian, B., and Ismail, S. O., 2022. Epoxy/hollow glass microsphere syntactic foams for structural and functional application-A review. *European Polymer Journal*, **171**, 111163.

[23] He, Z. Q., Yang, Y., Yu, B., Yang, J. P., Jiang, X. B., Tian, B., Wang, M., Li, X.Y., Sun, S.Q. and Sun, H., 2022. Research on properties of hollow glass microspheres/epoxy resin composites applied in deep rock in-situ temperature-preserved coring. *Petroleum Science*, **19**(2), 720-730.

[24] Anandakumar, P., Kanny, K., Mohan, T. P. and Velmurugan, R., 2024. Mechanical behavior of glass fiber‐reinforced hollow glass particles filled epoxy composites under moisture environment. *Polymer Composites*, 1-18.

[25] Paramasivam, A., Kanny, K., Turup Pandurangan, M. and Ramachandran, V., 2024. Mechanical behavior of glass fiber-reinforced hollow glass particles filled epoxy composites under thermal loading. *Journal of Composite Materials*, 00219983241259113.

[26] Garg, A. C., and Mai, Y. W., 1988. Failure mechanisms in toughened epoxy resins—a review. *Composites Science and Technology*, **31**(3), 179-223.

[27] Nielsen, L.E. 1993. *Mechanical Properties of Polymers and Composites*.

Marcel Dekker.

[28] Unnikrishnan, K. P., and Thachil, E. T., 2006. Toughening of epoxy resins. *Designed monomers and polymers*, **9**(2), 129-152.

[29] Domun, N., Hadavinia, H., Zhang, T., Sainsbury, T., Liaghat, G. H., and Vahid, S., 2015. Improving the fracture toughness and the strength of epoxy using nanomaterials–a review of the current status. *Nanoscale*, **7**(23), 10294-10329.

[30] Mousavi, S. R., Estaji, S., Paydayesh, A., Arjmand, M., Jafari, S. H., Nouranian, S., and Khonakdar, H. A., 2022. A review of recent progress in improving the fracture toughness of epoxy‐based composites using carbonaceous nanofillers. *Polymer Composites*, **43**(4), 1871-1886.

[31] Adachi, T., Araki, W. and Higuchi, M. 2010. Effect of silica particles on mechanical properties of epoxy composites (in Japanese). *Journal of the Adhesion Society of Japan*. **46**(6), 222-229.

[32] Milovanović, B. and Banjad Pečur, I., 2016. Review of active IR thermography for detection and characterization of defects in reinforced concrete. Journal of Imaging, **2**(2), 11.

[33] Hiasa, S., Birgul, R. and Catbas, F. N., 2017. Effect of defect size on subsurface defect detectability and defect depth estimation for concrete structures by infrared thermography. *Journal of Nondestructive Evaluation*, **36**(3), 57.

[34] Sirca Jr, G. F. and Adeli, H., 2018. Infrared thermography for detecting defects in concrete structures. *Journal of Civil Engineering and Management*, **24**(7), 508-515.

[35] Tomita, K., and Chew, M. Y. L., 2022. A review of infrared thermography for delamination detection on infrastructures and buildings. *Sensors*, **22**(2), 423.

[36] Hagiwara, T. and Suzuki, T. 2024. Non-contact evaluation of filling ratio of concrete crack repair material using hollow particle mixed resin by infrared thermography (in Japanese). *Proceedings of the Japan Concrete Institute*. **46**(1), 1891-1896.

[37] Japan Society of Mechanical Engineers. 1986. *JSME data book: heat transfer* (in Japanese). Maruzen Publishing.

[38] Japan Society of Civil Engineers. 2012. *Standard specifications for concrete structure* (in Japanese). Maruzen Publishing.

[39] Japan Society of Thermophysical Properties. 2008. *Thermophysical properties handbook* (in Japanese). Yokendo.

[40] Hagiwara, T., Shimamoto, Y., and Suzuki, T. (2024). Non-contact evaluation of corroded-steel-sheet-pile thickness using heat-balance simulation and infrared measurement (in Japanese). *Journal of JSCE No.2 Special issue (Applied Mechanics)*, 80(15), 23-15049.

[41] Shibano, K., Hagiwara, T., Kimura, M., Ohno, K., and Suzuki, T. (2024). Use of Passive Infrared Thermography Method for Subsurface Damage Evaluation of Dam Concrete by Integration of Image Clustering with Heat Balance Analysis (in Japanese), *Journal of Japan Society of Dam Engineers*, 34(2), 129-143.